The International Journal of Advanced Manufacturing Technology (2018) 97:4043–4054
https://doi.org/10.1007/s00170-018-2227-z

ORIGINAL ARTICLE

Tailoring corrosion resistance of laser-cladded Ni/WC surface by adding rare earth elements

Sayeed Mohammed[1] · Ravi Shanker Rajamure[2] · Zhe Zhang[1] · Prabu Balu[3] · Narendra B Dahotre[2] · Radovan Kovacevic[1]

Received: 14 February 2018 / Accepted: 21 May 2018 / Published online: 6 June 2018

Abstract
The corrosion is a major limiting factor for steel in the harsh environments and can be controlled by depositing protective passive coatings. Nickel-based alloy cladding of steel offers a solution by enabling better wear and corrosion resistance, and high bonding strength. The laser surface cladding of steel was conducted using a high-power direct diode laser. Layers of tungsten carbide in Ni (40% Ni-60% WC) combined with 1 and 2% lanthanum oxide (La_2O_3) and cerium oxide (CeO_2) were deposited on ASTM A36 steel substrate. The X-ray diffraction and scanning electron microscopy were employed to study the morphology, microstructure, and phase evaluation of the cladded layer. Further, anodic polarization on the laser-cladded coupons in 3.5 wt% NaCl shows significant enhancement of the corrosion resistance. The addition of La_2O_3 and CeO_2 improves the corrosion resistance and the hardness of the clad.

Keywords Corrosion resistance · Laser cladding · Ni-WC · Rare earth elements

1 Introduction

Steel is most widely used material in engineering applications but its hardness, wear, and corrosion resistance limit its applications in the extreme conditions. The choice of corrosion control depends on economics, the environments, and the technical limitations. The protective coating is the most popular method to control the corrosion resistance [1]. With the advances in the technology and the emphasis on the reduced cost, the laser has received significant attention in the areas of high-value component repair such as drill bits, turbine and compressor blades, the rollers for rolling mills, and the engine pistons [2]. For example, the oil and gas industry uses drill bits which are constantly subjected to harsh environments and special conditions. The wear and gouging accelerate the deterioration of the properties and structure of the bits [3]. The laser cladding is widely used to solve such problems by improving hardness, wear, and corrosion resistance resulting in improved service lifetime. The conventional laser sources are Nd:YAG, fiber, CO_2, and diode laser. In the high-power direct diode laser, the beam size and shape can be varied. Kennedy et al. [4] found that diode laser has better modal stability than CO_2 or Nd:YAG laser. Zhu et al. [5] reported that the porosity of welds by diode laser was less as compared to that of CO_2 laser welding. Due to its high power, the laser cladding produces metallurgically bonded coatings having little distortion of the substrate [6]. The development of high-power diode laser opened new frontiers for metal hardening, welding, and cladding. The laser cladding was an ideal solution for the substrates of complex geometry. The substrate can be designed for toughness and strength and the coating for the hardness, wear, and corrosion resistance [7]. Although the first working laser was invented by Maiman [8] in 1960, the laser cladding was not applied until the 1970s by Gnanamuthu at Rockwell International Corporation, California [9].

Corrosion is an electrochemical phenomenon which results in deterioration of physical properties of the material due to reaction with its environment. The corrosion is a diffusion-

✉ Radovan Kovacevic
kovacevi@lyle.smu.edu

[1] Research Center for Advanced Manufacturing, Department of Mechanical Engineering, Southern Methodist University, Dallas, TX 75205, USA

[2] Laboratory for Laser Materials Processing and Synthesis, Department of Materials Science and Engineering, University of North Texas, Denton, TX 76203, USA

[3] Coherent Inc., Santa Clara, CA 95051, USA

controlled process and occurs more or less uniformly by the formation of pits causing relatively rapid penetration at small discrete areas [10]. The corrosion requires an anodic reaction, where electrons are released; a cathodic reaction, where electrons are absorbed; and a medium called electrolyte for electron transport. The Ni-based alloys combined with other reinforced particles have become very attractive due to their excellent wear and corrosion resistance [11]. The combination of the mechanical properties of Ni and WC makes Ni-WC most desirable in the engineering applications having harsh environments with high loads [12]. The corrosion resistance of steel improves effectively by laser cladding of 304ss/Al_2O_3 composite coating on its surface [13]. The cracks and pores are often observed in overlapping region of the coatings with metallurgical bond to the substrate [14]. The corrosion behavior of steel depends on the aging and composition of the coating [15]. A more porous coupon suffers more corrosion because of the greater surface area exposed to the environment [16]. The corrosion behavior of a surface depends on the presence of local heterogeneity in the microstructure over the various scales such as (1) mesoscale or relative surface roughness; (2) macroscale such as grain refinement, segregation, and presence of various phases, compositional variation; (3) nanoscale-like dislocation density, configuration, and grain refinement; and (4) chemical bonding for instance, covalent, ionic, or metallic bonding [17].

Thermal barrier coatings (TBC) are applied on the high-performance components to extend their service life. TBCs tolerate hot corrosion better particularly with acidic stabilizer CeO_2 and laser glazing prevent salt penetration [18]. TBCs consist of a top coat (TC) for thermal barrier, and a bond coat (BC) to produce adhesion for TC and to resist oxidation. The rare earth element, Yttria partially stabilized zirconia (ZrO_2 with 6–7 wt% Y_2O_3), is used in TC as it possess a comparable thermal expansion with the substrate and low thermal conductivity [19]. In electronics industry, Ytterbium-doped fiber is used for modulation in optical switching [20]. It was found that Yb^{3+}-doped fiber decreases the switching power under 20 mW by parameter optimization of fiber Bragg grating [21]. The rare earth elements are popular in the manufacturing of high-performance magnets used in radar system for high-temperature applications. The oxide of rare earth element CeO_2 (cerium oxide or ceria) works as a reducible oxide agent in catalytic reactions [22]. The oxide of rare earth element, La_2O_3 (lanthanum oxide or lanthana) has been used in laser sintering metal matrix processing. The addition of La_2O_3 up to 1.0 wt% increases homogeneity of particulate dispersion and the amount more than 1.5 wt% produces a heterogeneous microstructure and retards the activity of La_2O_3 [23]. The rare earth elements La and Ce have large atomic radii of 0.188 and 0.182 nm and lower electronegativities of 1.1 and 1.05 respectively. They enable them to form ions (La^{3+}, Ce^{3+}) and those are likely to react with other elements easily. La_2O_3 and CeO_2 can significantly enhance the high-temperature behavior and mechanical properties of metals due to their rare chemical properties. La_2O_3 and CeO_2 are readily available as compared to that of Yttria. The use of these rare earth elements in laser cladding has broadened their applications. Wang et al. [24] investigated the effects of La_2O_3 and CeO_2 on Ni-based alloy ranging from 0 to 8 wt%. It was reported that the use of La_2O_3 and CeO_2 greater than 4 wt% was not suitable for corrosion resistance [25]. In the rare earth modified Ni/WC coatings, the hardness increased with 0.9 wt% CeO_2 and porosity decreased with 0.6 wt% CeO_2 as compared to conventional Ni/WC coatings [26]. Therefore, the amount of rare earth elements in the clad is critical. If not added in the right amount, they can change the chemistry noticeably. After a thorough literature survey on corrosion resistance, it was found that not much had been reported for 1 wt% or larger addition of La_2O_3 and CeO_2 in 40 wt% Ni-60 wt% WC clad of thickness of 1 mm or more. In view of this, the authors are motivated to study the influence of 1 and 2 wt% La_2O_3 and 1 and 2 wt% CeO_2 on the corrosion resistance and hardness of Ni/WC clad. A large sample size of 50 coupons was used to substantiate the findings. The current study was performed with SEM, X-ray diffraction (XRD), a microhardness tester, and a computer-controlled potentiostat using 3.5 wt% NaCl solution.

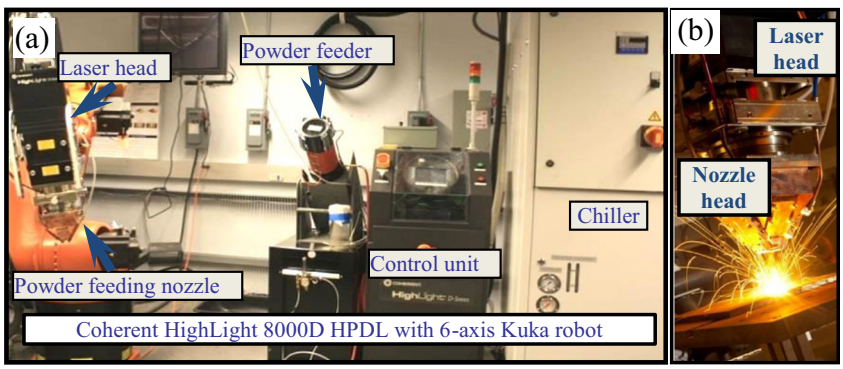

Fig. 1 **a** Experimental setup. **b** Close-up of the laser head

Table 1 Chemical composition, percent by weight, of ASTM A36 [27]

Elements	C	Si	Mn	S	P	Ni	Cu	Fe
% by weight	0.26	0.40	0.75	0.05	0.04	0.01	0.20	98.29

2 Experimental study

2.1 Experimental setup

The experimental setup is shown in Fig. 1 that consists of a direct diode laser of 8 kW in power, a powder feeder, a chiller to cool laser head and a laser itself, and powder feeding nozzles. The laser head is mounted on 6-axis Kuka robotic arm. The powder is delivered by symmetric co-axial powder feeding nozzles to the focal point of the laser beam using argon as carrier gas. The area around the clad is also protected from oxidation by argon as shielding gas. The robotic arm is programmed to move the laser head to the cladding position on the coupon and travel for a length of 33 mm. The laser head is inclined at an angle of 10° in order to avoid a harmful back reflection of the laser beam. A high-power direct diode laser of 980-nm wavelength with a maximum power of 8 kW was used for cladding. The laser spot is a top-hat distribution of a rectangular shape with 12 mm × 1 mm in size. The top-hat has uniform intensity across the rectangular cross-section as opposite to a circular spot where intensity is higher at the center and follows a Gaussian distribution. From our previous studies, the key process parameters were identified as powder flow rate, scanning speed, and the laser power. For clads to have minimum porosity, the experiments are conducted at a laser power of 2600 W, at powder flow rate of 0.9 g/s, and a scanning speed of 6 mm/s.

2.2 Material and coupon preparation

Mild steel A36 of the dimensions 100 mm × 100 mm × 10 mm was used as the substrate. The substrate chemical composition is summarized in Table 1.

ASTM A36 coupons were grinded to achieve a smooth surface. The grinded substrates were sand blasted for improving laser absorption efficiency. They were further cleaned with acetone to remove contaminates. The coupons were dried in a furnace at 100 °C for 1 h to remove the moisture. The Coherent Highlight D-series laser head and the fixture were thoroughly cleaned to avoid any contamination. The tungsten carbide powder consisted of WC and W_2C with grain size ranging from 80 to 160 μm. The Ni powder had 4.5% Si, 2.9% B, and 92.6% Ni with grain size varying from 1 to 60 μm. The morphology of powder consisted of crushed particles instead of globular as shown in Fig. 2a. The powder was dried in a furnace at 250 °C for a period of 6 h. The experiments were planned for cladding with a number of combinations of alloying elements as presented in Table 2. Each combination was thoroughly mixed and homogenized in a powder-mixing device. The mixture was loaded in the powder feeder.

After cladding, the coupons were cross-sectioned and mounted in EZ epoxy resin with hardener. They were grinded and polished on silicon carbide papers ranging from 120 to 1200 grit size. The coupons were further polished on a rotating wet velvet cloth disk using diamond suspension of 1-μm particle size to a shining reflective surface. The polished surface was etched with $3HCl + 1HNO_3$ for microstructure analysis [28].

2.3 SEM and XRD analysis

The clads were examined on an environmental scanning electron microscope (ESEM) FEI Quanta 200 machine. The ESEM is fitted with secondary electron and back-scattered electron detectors. The cross-section micrographs of the cladded coupons were recorded. The micrographs were taken at the magnifications of × 50, × 200, and × 500. The XRD was conducted on Rigaku II Ultima X-ray diffractometer in a 2θ range of 20°–90° operating at 40 kV and 44 mA. The step size of 0.02°, scan speed of 4°/min, and the wavelength of 0.15148 nm for Cu Kα radiation were used. The sets of data were plotted. The peaks were compared with the diffraction data files for phase identification. The files are international

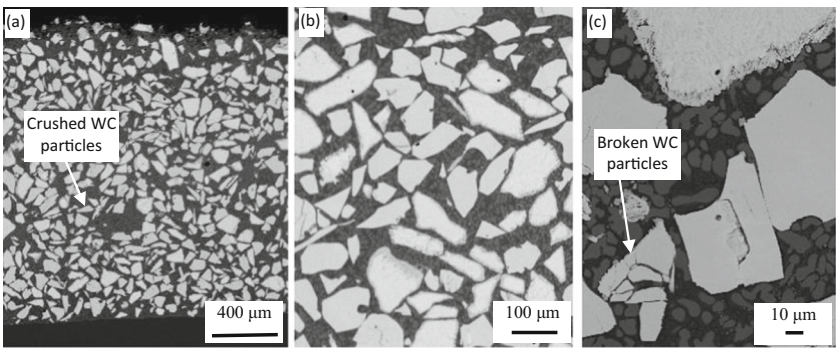

Fig. 2 Back-scattered cross-sectional SEM micrographs of 40 wt% Ni-60 wt% WC clad layer. **a** Clad × 50; **b** WC particles of different sizes, × 150; and **c** broken particles of WC, × 500

Table 2 Chemical contents of clads, percent by weight

Coupon identification no.	La_2O_3	CeO_2	Ni	WC
1	1	–	39	60
2	2	–	38	60
3	–	1	39	60
4	–	2	38	60

standards and are established by Joint Committee of Powder Diffraction Standards (JCPDS).

2.4 Electrochemical analysis

The potentiodynamic polarization test is an electrochemical corrosion measurement technique to study the corrosion behavior. In this technique, the electrode potential is changed and the current is monitored relative to time. The anode process is governed by activation polarization control and the cathode process is governed by the oxygen diffusion [29].

Anodic potentiodynamic polarization (APP) experiments were performed in naturally aerated condition at standard temperature using a classic three-electrode conventional flat cell containing 3.5 wt% NaCl solution prepared from ultra-pure deionized water. The cell was equipped with two graphite rods, one as a counter electrode, and the other as a saturated calomel electrode (SCE) or reference electrode. The cladded coupon acts as a working electrode with an area of 1 cm × 1 cm. After polishing, the coupons were cleaned in ultra-sonic bath using methanol and deionized water separately for 5–15 min. The APP tests were performed in a near neutral pH conditions (pH 6.91 ± 0.25) with Versa II potentiostat from EG & G Instruments, Princeton Applied Research, Oak Ridge, Tennessee. Before commencement of scan, an open circuit potential (OCP) was stabilized for 1 h. After achieving the stable state, a scan was initiated by increasing the potential with at 1 mV/s in the anodic direction, from − 150 mV (SCE) relative to OCP and the scan was terminated at the final potential of + 100 mV (SCE) [30]. From the polarization plot, the corrosion current density (I_{Corr}), corrosion potential (E_{Corr}), and anodic (β_a) and cathodic (β_c) slopes were evaluated by using Tafel extrapolation method [31]. E_{Corr} depicts the stability of the surface thermodynamically in the exposed corrosive environment. I_{Corr} determines the degree of corrosion rate. To check reliability and reproducibility of results, the corrosion experiments were repeated at least three times and the data was averaged and reported in this paper.

3 Results and discussion

3.1 Microstructure and morphological observations

The cross-sectional SEM micrographs of 40 wt% Ni-60 wt% WC shown in Fig. 2 elucidate the morphology of the clad layer. The buckling or delamination of the clad was not observed. For all the clads, a sharp interface was noticed which can be attributed to the fact that there was no dilution or dissolution of alloying elements into the substrate (Fig. 2a). Within the clad layer, the WC particles of different sizes and shapes are observed (Fig. 2b). The WC particles were ingrained in the Ni alloy matrix. The microstructure consists of white WC particles and precipitated carbides diffused in the Ni matrix. The higher atomic number of W, as compared to the other elements, generates striking contrast in SEM micrographs. The clads were found to be free of cracks and characterized by excellent adhesion to the substrate, having minimum porosity. The clad layer was compact and well bonded to substrate. Due to the large variation in the thermal mismatch among the alloying elements, partial melting and broken particles of WC were also noticed in the clad (Fig. 2c).

The clad morphology for 39 wt% Ni-60 wt% WC-1 wt% La_2O_3 is shown in Fig. 3. The crystal nucleation is observed around the WC particles (Fig. 3b).

The cross-sectional SEM micrographs of 38 wt% Ni-60 wt% WC-2 wt% La_2O_3 is shown in Fig. 4. The crystal nucleation around the WC particles was still presented.

The clad morphology of 39 wt% Ni-60 wt% WC-1 wt% CeO_2 is shown in Fig. 5. The crystal nucleation around the

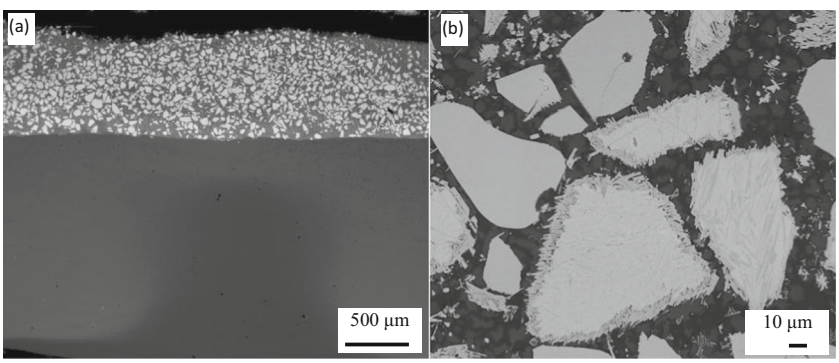

Fig. 3 Back-scattered cross-sectional SEM micrographs of 39 wt% Ni-60 wt% WC-1 wt% La_2O_3 clad. **a** Low magnification view. **b** High magnification view

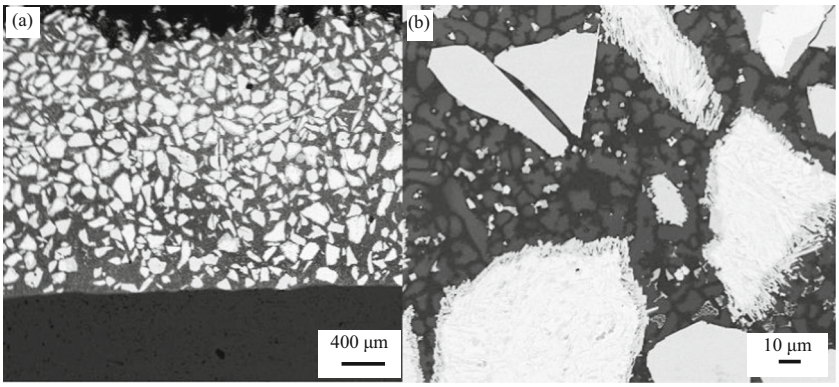

Fig. 4 Back-scattered cross-sectional SEM micrographs of 38 wt% Ni-60 wt% WC-2 wt% La_2O_3 clad. **a** Low magnification view. **b** High magnification view

WC particles was much less as compared to 38 wt% Ni-60 wt% WC-2 wt% La_2O_3.

The cross-sectional SEM micrographs of 38 wt% Ni-60 wt% 2 wt% CeO_2 is shown in Fig. 6. The degree of crystal nucleation around the WC particles was more as compared to that of 39 wt% Ni-60 wt% 1 wt% CeO_2.

3.2 Phases and chemical compositions

The XRD spectra of the substrate, 40 wt% Ni-60 wt% WC, and with 1 and 2 wt% La_2O_3 and 1 and 2 wt% CeO_2, are shown in Fig. 7 (f), (e), (d), (c), (b), and (a) respectively. In XRD, the detector position is recorded as the angle two-theta, the angle between diffracted ray, and the incident ray. The diffracted signals are converted into peaks for each two-theta angles for a known wavelength of X-ray. The peaks were identified in terms of the number of detected photons (counts). The position of XRD peak depends on the orientation of crystal, lattice type, and crystallite size. The intensity of peaks determines the type of atoms and position of atoms. Using Bragg's law, the family of lattice planes (hkl) are determined for each peak. The recorded data is compared with the reference peaks in JCPDS files. In Fig. 7 (f), the sharp diffraction peaks for planes (110), (200), and (211) in the substrate XRD found to be for ferrite (α-Fe) cubic lattice. The diffraction peaks for carbide phase in steel were not visible because XRD can identify phases only if they were more than 5% [32]. In Fig. 7 (e), a sharp peak for planes Ni(111) C(111) was observed in Ni-WC XRD as iron and nickel have almost identical atomic diameters and both crystallize in the face-centered cubic system. In accordance with previous studies, the XRD shows the presence of other various phases in the clad layer mainly W_3C, W_2C, WC, Ni, and C. The intermetallic phases were formed because of very high energy density of the laser resulting in high microhardness. In Fig. 7 (d)–(a), the addition of surface reactive rare earth element oxides La_2O_3 and CeO_2 produced new phases La_2NiO_2, $La_2Ni_5C_3$, and $Ce_2(WO_4)_3$ [33]. Further, the changes in the diffraction peak intensities were observed due to the addition of rare earth oxides. There are some smaller peaks from 55° to 63° which did not match with peaks in JCPDS, so left unmarked. There are very minor peaks beyond 85° that can be attributed to background noise [34].

3.3 Vickers hardness measurements

The hardness is dictated by a combination of extrinsic properties such as stress fields, morphology, and defects, and intrinsic properties such as bond strength, crystal structure, and cohesive energy [35]. From a macroscopic view point, the hardness is evaluated by the materials' elastic moduli. From a microscopic perspective in a crystal, the hardness is determined by the associated strength of chemical bonds to indentation [36]. The Vickers microhardness of substrate, 40 wt% Ni-60 wt% WC, and with La_2O_3 and CeO_2 coupons, was measured on Clark Microhardness Tester (CM-700AT) for

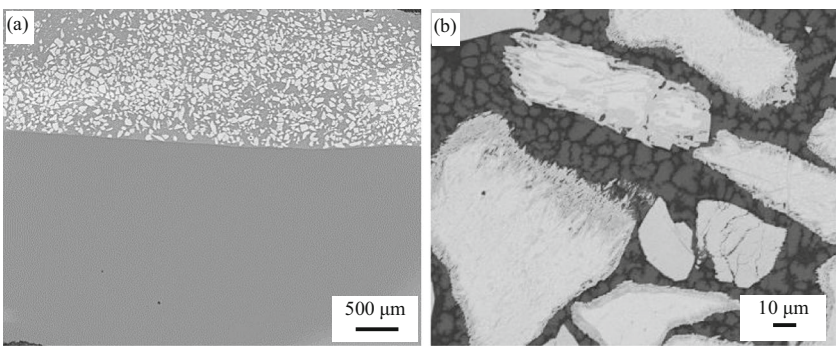

Fig. 5 Back-scattered cross-sectional SEM micrographs of 39 wt% Ni-60 wt% WC-1 wt% CeO_2 clad. **a** Low magnification view. **b** High magnification view

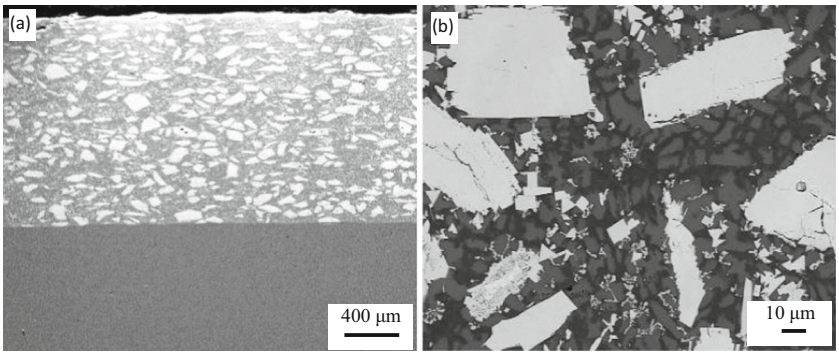

Fig. 6 Back-scattered cross-sectional SEM micrographs of 38 wt% Ni-60 wt% WC-2 wt% CeO_2 clad. **a** Low magnification view. **b** High magnification view

15 s and 300 GF load. The averages of readings at eight locations across the clad for six coupons are plotted in Fig. 8 for each condition. The hardness of substrate was found to be 152 HV as compared to the average hardness of 478 HV for cladded coupons. The lower microhardness of substrate is attributed to its metallic bonds which are weaker mainly due to their non-directionality. The high hardness of 40 wt% Ni-60 wt% WC clad is attributed to the higher bond density and the greater three-dimensional network structures of covalent bonds. The directionality of covalent bonds impedes the dislocation motion and restricts the plastic deformation [37]. While cladding, the WC particles are dissolved and reprecipitated in the matrix as finer carbide particles resulting in higher hardness. The average microhardness of 1 wt% La_2O_3 and 2 wt% La_2O_3 were almost the same and so does for 1 wt% CeO_2 and 2 wt% CeO_2, but the average microhardness of

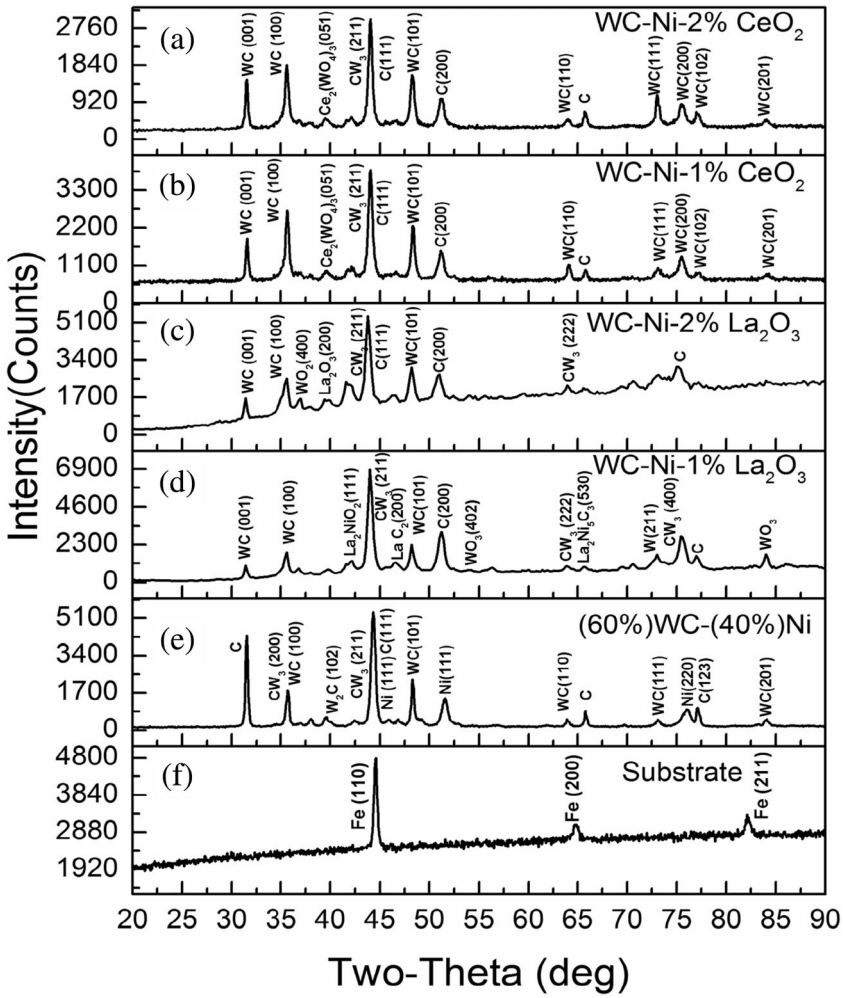

Fig. 7 XRD spectra of substrate and laser-cladded coupons (a), (b), (c), (d), (e), and (f)

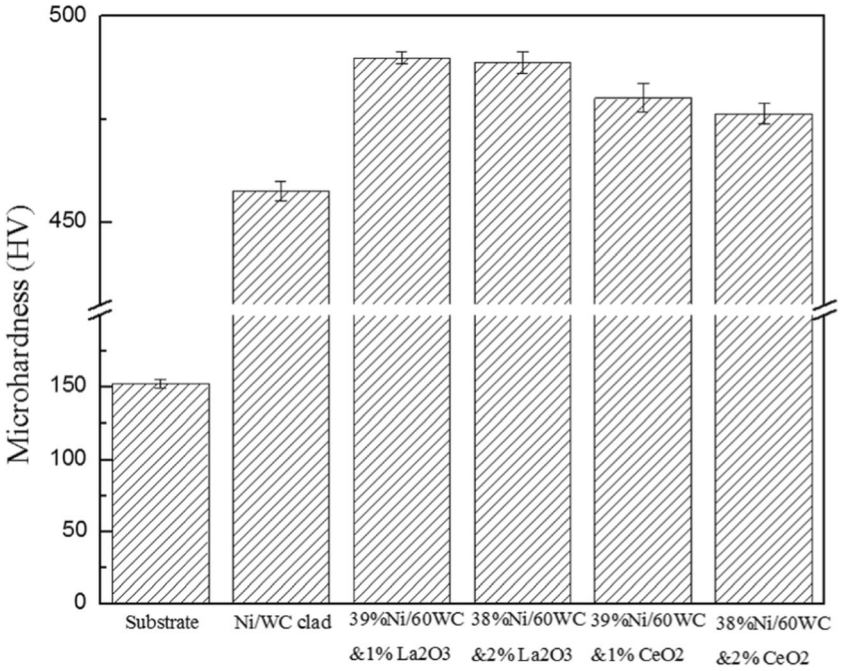

Fig. 8 Microhardness under different chemical compositions

1 wt% La_2O_3 and 2 wt% La_2O_3 was more than for 1 wt% CeO_2 and 2 wt% CeO_2, respectively. The microstructure refinement due to the addition of rare earth elements further led to an increase in surface hardness. The refinement introduces more and more grain boundaries that halt the movement of dislocations between grains. The covalent and polar covalent bonding generates low plasticity and high hardness [38]. The addition of La_2O_3 and CeO_2 promotes the covalent bond formation improving the hardness of the laser clad. The lanthanides have low ionization potential enabling an ionized atom with a smaller atomic radius. Further, the lanthanide ions are partially dissolved causing an increase in the nucleation rate and decrease in crystal growth velocity. The surface hardness improvement is attributed to solid solution strengthening and the dispersion of finer particles. The increase in hardness by the addition of rare earth oxides can also be attributed to the production of W- and carbide-enriched domains. In spite of the fact that the rare earth elements have been called the "vitamin" of metals [23], their percentage amount is very important. From the one side, addition of these elements affects the resistance to corrosion and from the other side improves the hardness.

3.4 Corrosion resistance evaluation in 3.5 wt% NaCl

Stern-Geary Eq. (1) was used to compute polarization resistance (R_p) [30]. The coating efficiency (C_{EF}) was also calculated from Eq. (2) and used in the analysis.

$$R_p = \frac{\beta_a \beta_c}{2.3(\beta_a + \beta_c) I_{Corr}} \tag{1}$$

$$C_{EF} = \frac{I_{Corr}(\text{untreated}) - I_{Corr}(\text{laser cladded})}{I_{Corr}(\text{untreated})} \times 100\% \tag{2}$$

The formation of passive region/pit nucleation resistance was represented by the difference between ($E_{Pitp} - E_{Corr}$). In general, the formation of passive region indicates the resistance towards pitting corrosion. The various electrochemical

Table 3 Data extrapolated from Tafel and anodic polarization curves

Specimen	E_{Corr} (mV_{SCE})	I_{Corr} ($\mu A/cm^2$)	β_a (mV/decade) vs SCE	β_c (mV/decade) vs SCE	C_{EF} (%)	R_p (KΩ cm^2)
Substrate	− 620 ± 1.51	3.01 ± 0.08	141 ± 0.92	137 ± 1.10	0 ± 2.06	10.04 ± 0.77
40% Ni + 60% WC	− 442 ± 1.01	0.50 ± 0.05	48 ± 1.07	38 ± 3.61	83.39 ± 2.52	18.44 ± 1.19
39% Ni + 60% WC + 1% La_2O_3	− 348 ± 1.19	0.10 ± 0.08	37 ± 0.66	31 ± 1.83	96.68 ± 4.00	73.34 ± 1.87
38% Ni + 60% WC + 2% La_2O_3	− 409 ± 2.11	0.30 ± 0.05	103 ± 0.69	98 ± 2.72	90.03 ± 2.86	72.78 ± 0.97
39% Ni + 60% WC + 1% CeO_2	− 371 ± 1.15	0.32 ± 0.05	79 ± 0.82	67 ± 1.84	89.37 ± 2.79	49.26 ± 0.84
38% Ni + 60% WC + 2% CeO_2	− 413 ± 1.07	0.46 ± 0.07	106 ± 0.95	96 ± 2.37	84.72 ± 3.61	47.61 ± 0.89

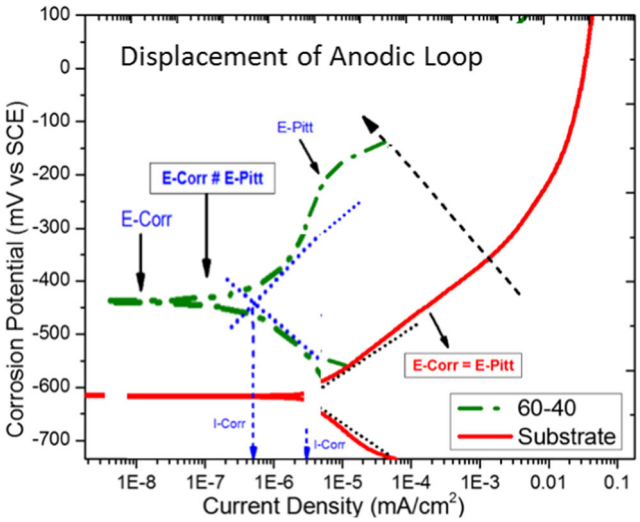

Fig. 9 APP curves of the substrate and laser-cladded coupons (60 wt% WC–40 wt% Ni) in 3.5 wt% NaCl solution

results extracted from the anodic polarization curves are presented in Table 3. The APP behavior of the substrate and laser-cladded coupons is presented in Fig. 9. It was noticed that after laser cladding, the corrosion parameters E_{Corr}, E_{Pitp}, I_{Corr}, anodic and cathodic slopes, coating efficiency, and polarization resistance were substantially affected. These variations were attributed to many factors such as grain size reduction, exotic microstructure, local microgalvanic effect between the alloying elements presented in the clad layer, intermetallics presented or evolved during laser cladding, their variation in volume fraction, and distribution within the clad.

It was noticed from the data of Table 3 that the R_p varied inversely with the corrosion rate. The greater value of R_p resulted in the greater corrosion resistance. The substrate had a significantly lower corrosion resistance because of higher current density and lower corrosion potential. Further, the pitting potential was coincided with the corrosion potential ($E_{Corr} = E_{Pitp}$, as marked on the curve for the substrate in Figs. 11 and 12) that indicated that the substrate did not exhibit the passivation behavior in 3.5 wt% NaCl solution. Besides, due to the absence of passivity in the anodic domain, the pitting was happening right from the beginning. The absence of passivity was caused by the local rupture of oxide layer in 3.5 wt% NaCl environment. The chloride ion attack caused the disintegration of oxide film resulting in pitting attack and subsequent conditions did not allow the passive region to be formed. The aggressive chloride ions ruined the passivity and promoted not only local depassivation but also localized corrosion. Therefore, the likelihood of extensive pitting corrosion was very high and its consequence is seen in Fig. 10. The localized morphology of the pitting attack on the substrate surface further showed that the pitting attack was higher. The SEM micrographs showed the penetration of pits into the substrate (Fig. 10a) and the resulting pitted surface (Fig. 10b). The spreading of pits on the surface creates hostile conditions which weakened the stability of oxide layer and caused extensive localized attack and further growth of pits of different sizes.

The corrosion resistance of the clad mainly depends on the alloying elements presented in the clad layer. The electrochemical properties of hard-phase WC are nobler than that of the Ni matrix; hence, the resulting galvanic corrosion of less noble element was mainly dependent on the variation of corrosion potential of the elements presented within the clad layer. For the clad 40% Ni-60% WC, the coating was mainly dominated by variants of WC phases and minor portion of Ni and C. The APP behavior showed considerable improvement in corrosion resistance because of the displacement of anodic loop towards lower corrosion current densities and also enhancement in $E_{Corr.}$ The positive displacement in E_{Corr} towards nobler potential −442 mV (SCE) indicated that there was an improvement in E_{Corr} to about 178 mV when compared to the substrate. Further, it was also illustrated that E_{Pitp} was not superimposed with E_{Corr} [39]. The E_{Pitp} at − 144 mV (SCE) elucidated the presence of passive behavior of about 298 mV (SCE). The passive region indicated that there was a substantial reduction in the number of breakdown points. Therefore, the length of the passivity was longer. The presence of these phases curtailed

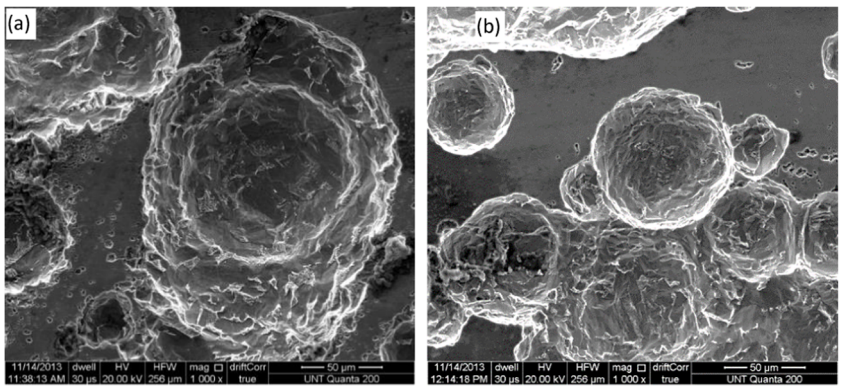

Fig. 10 Localized morphology of the pitting attack. **a**, **b** Wider and deeper pitting attacks into the substrate

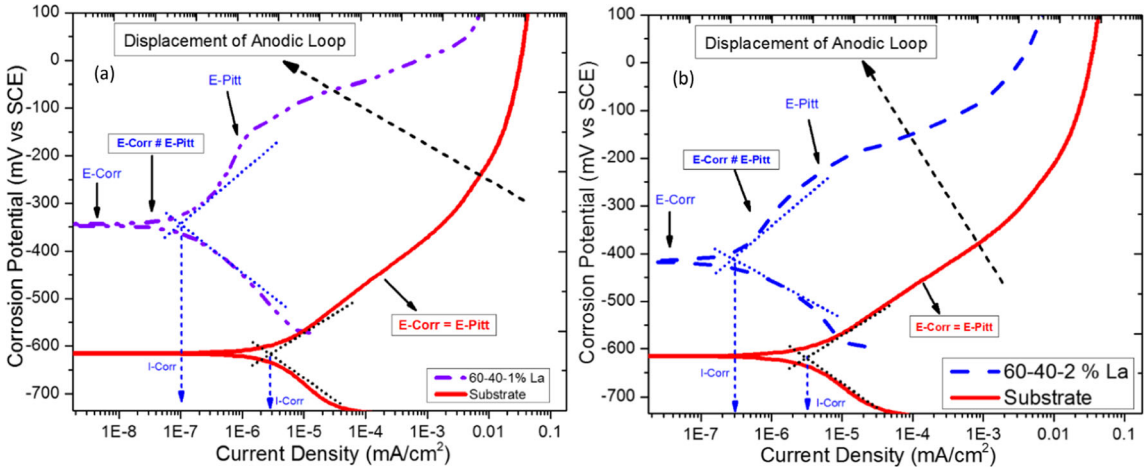

Fig. 11 APP curves of laser-cladded coupons. **a** 39 wt% Ni-60 wt% WC-1 wt% La_2O_3 and **b** 38 wt% Ni-60 wt% WC-2 wt% La_2O_3 in 3.5 wt% NaCl solution

the number of anodic sites on the clad surface which would reduce the anodic reaction rate. After the E_{Pitp}, there was an increase in the corrosion potential in the transpassive region, which showed the occurrence of corrosion.

In 40 wt% Ni-60 wt% WC condition, the improvement in corrosion resistance was shown by the low value of I_{Corr}. The substantial change in the nature of morphology after laser cladding was caused by the presence of the phases in the alloyed layer which evolved during laser cladding. The higher values of polarization resistance, R_p, and coating efficiency, C_{EF}, for 40 wt% Ni-60 wt% WC clad as compared to that for the substrate in Table 3 verified the result.

The results for the addition of 1 and 2 wt% of La_2O_3 are shown in Figs. 11a, b respectively. The displacement of anodic loop tends to increase as compared to that of 40 wt% Ni-60 wt% WC clad. APP behavior showed an improvement in corrosion resistance by the displacement of anodic loop towards lower corrosion current densities and enhancement in E_{Corr} more than that for 40 wt% Ni-60 wt% WC clad. For instance, the corrosion current density for 1 wt% of La_2O_3 clad had dropped to 0.10 μA/cm^2 as compared to 0.5 μA/cm^2 for 40 wt% Ni-60 wt% WC clad. This indicated that the corrosion resistance increased further by the addition of La_2O_3. The polarization resistance for 1 wt% La_2O_3 in Table 3 was drastically improved as compared to that of 40 wt% Ni-60 wt% WC clad. The polarization resistance for 1 wt% La_2O_3 was slightly more than that for 2 wt% La_2O_3 and so did the protective efficiency. It was indicated that the optimum composition of La_2O_3 for impeding interdendritic spacing, the number of inclusions, and improving corrosion resistance was somewhere between 1 to 2% of La_2O_3.

The results for the addition of 1 and 2 wt% CeO_2 are shown Figs. 12a, b respectively. APP behavior shows an improvement in corrosion resistance through the displacement of anodic loop towards lower corrosion current densities and

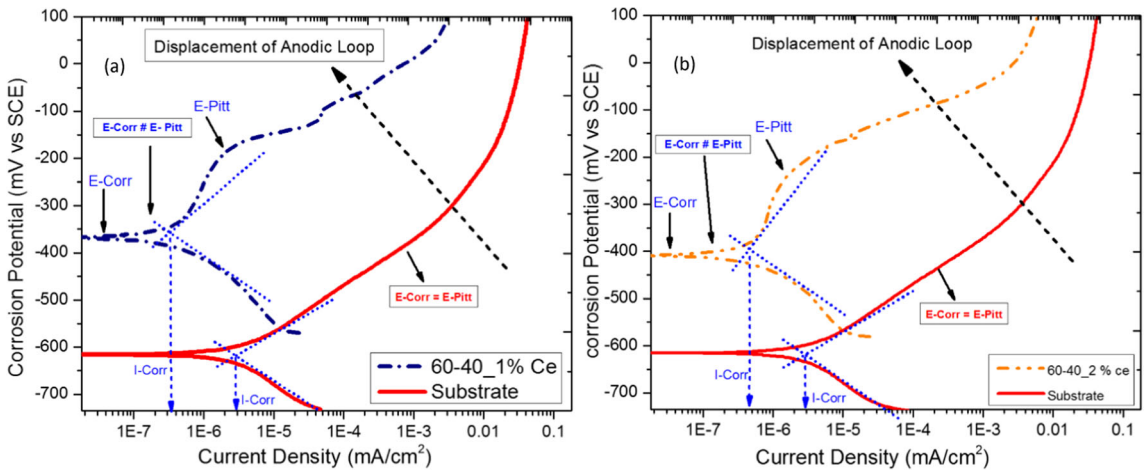

Fig. 12 APP curves of the laser-cladded coupons. **a** 39 wt% Ni-60 wt% WC-1 wt% CeO_2 and **b** 38 wt% Ni-60 wt% WC-2 wt% CeO_2 in 3.5 wt% NaCl solution

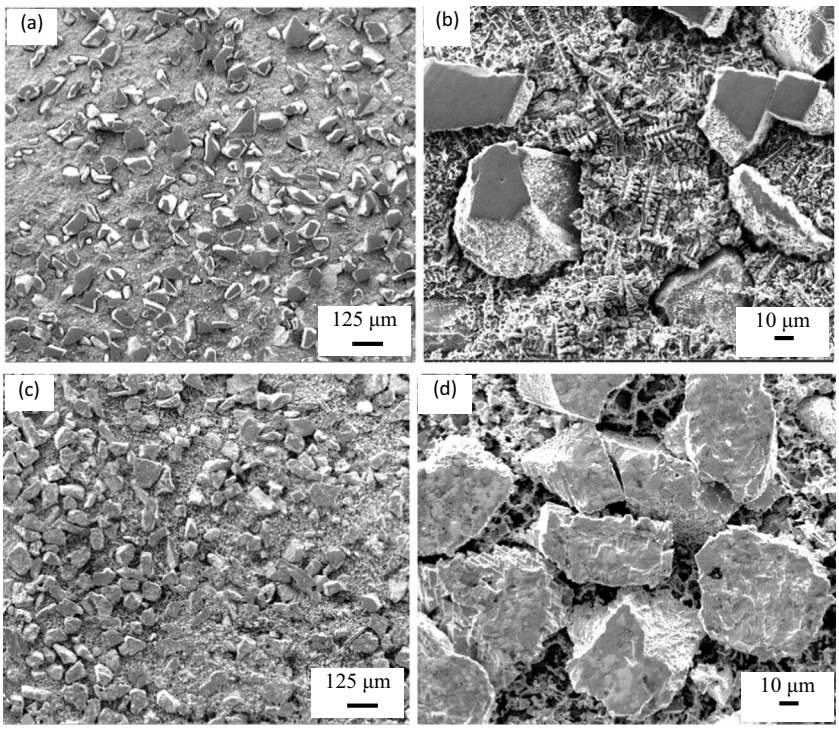

Fig. 13 Corroded morphology of **a** smaller and **b** larger scale for 39 wt% Ni-60 wt% WC-1 wt% La_2O_3, and **c** smaller **d** larger scale for 38 wt% Ni-60 wt% WC-2 wt% La_2O_3 obtained after anodic polarization in 3.5 wt% NaCl

enhancement in E_{Corr} more than that for 40 wt% Ni-60 wt% WC clad. In case of 1 wt% CeO_2, the corrosion current density dropped to 0.32 μA/cm^2 indicating that the corrosion resistance increases by the addition of CeO_2. The polarization resistance for 1 wt% CeO_2 was slightly more than that for 2 wt% CeO_2 and so did the protective efficiency. That further led to the notion that the optimum composition for improving corrosion resistance was somewhere between 1 to 2% of CeO_2. The increase in polarization resistance and protective efficiency for 1 wt% La_2O_3 and 2 wt% La_2O_3 was more than those for 1 wt% CeO_2 and 2 wt% CeO_2 respectively. It was concluded that the increase in corrosion resistance by the addition of La_2O_3 was more than that by the addition of CeO_2.

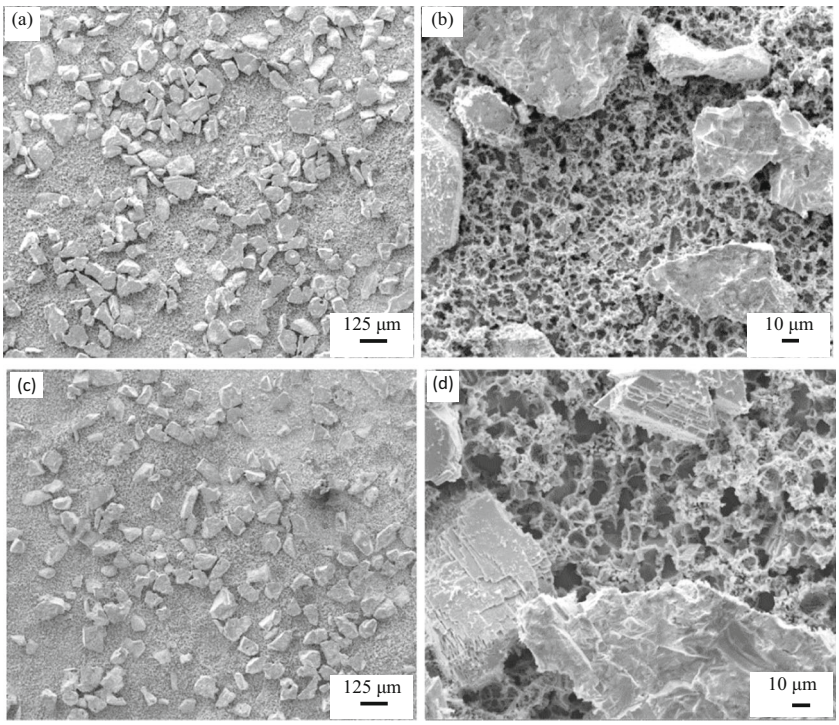

Fig. 14 Corroded morphology of **a** smaller and **b** larger scale for 39 wt% Ni-60 wt% WC-1 wt% CeO_2, and **c** smaller and **d** larger scale for 38 wt% Ni-60 wt% WC-2 wt% CeO_2 obtained after anodic polarization in 3.5 wt% NaCl

The Figs. 13a, b and 14c, d exhibit the transformed morphologies by the addition of 1 wt.%, 2 wt.% La_2O_3 and 1 wt.%, 2 wt.% CeO_2 respectively. The increase in corrosion resistance can be attributed to the grain refinement aided by rare earth elements [40]. They facilitate the formation of a greater number of grains and so does the number of crystal nuclei restricting the size of the grain. Due to their large atomic radii, they spread largely on the grain boundary hampering the grain growth further [41].

The microstructure was transformed from coarse to fine grain structure and no columnar crystals were observed. The interfacial morphology resulted in limited snowflake structures. In case of La_2O_3, extremely small equiaxed dendritic arm spacing was observed (Fig. 13b) but insignificant in the case of CeO_2 (Fig. 14b). This indicated that the addition of rare earth oxides impedes the formation of dendrites and columnar crystals as reported in our previous studies [42]. During laser cladding, the rapid heating and solidification caused microstructural changes [43]. Moreover, the phases which were evolved during laser cladding due to extremely high thermal power were predominantly carbide compounds WC, W_3C, and W_2C which are highly covalent in nature. The evolution of complex phases such as WC, W_3C, and W_2C showed the chemical stability and formation of a passive region in the chloride-rich medium. Hence, the increase in corrosion resistance was because of the existence of networks of covalent bonds and complex structures.

4 Conclusions

In this study, the corrosion resistance and hardness of 40% Ni-60% WC clad with the additions of 1 and 2% La_2O_3, and 1 and 2% CeO_2 were investigated. The following conclusions could be made:

In microstructure analysis, a consistent WC phase distribution was detected. The microstructure refinement of the clad can be attributed to the unique characteristics of La_2O_3 and CeO_2. The clad was bonded to the substrate with distinct interface. At the interface of the clad and substrate, a planar solidification was observed.

The microhardness of the coupons with 40% Ni-60% WC coating was significantly improved as compared to that of the substrate. The addition of La_2O_3 and CeO_2 improved hardness further slightly. The increase in the hardness by the addition of La_2O_3 was more pronounced than that for CeO_2.

The corrosion resistance of 40% Ni-60% WC clad was significantly improved as compared to that of the substrate. The addition of 1 wt% La_2O_3 increased the corrosion resistance and appeared to get optimized below 2 wt% La_2O_3 and so does for CeO_2. The addition of La_2O_3 or CeO_2 increased the corrosion resistance as compared to that for 40% Ni-60% WC clad. The addition of La_2O_3 increased the corrosion resistance more than that by CeO_2 addition.

Acknowledgments The authors would like to thank Andrzej Socha, a research engineer at RCAM, for his assistance in conducting the experiments.

Funding information This work was financially supported by the Research Center for Advanced Manufacturing (RCAM) at SMU.

References

1. Huang SW, Samandia M, Brandt M (2004) Abrasive wear performance and microstructure of laser clad WC/Ni layers. Wear 256(11–12):1095–1105
2. Guo C, Chen J, Zhou J (2012) Effects of WC-Ni content on microstructure and wear resistance of laser cladding Ni-based alloys coating. Surf Coat Technol 206(8–9):2064–2071
3. Kembaiyan KT, Keshavan K (1995) Combating severe fluid erosion and corrosion of drill bits using thermal spray coating. Wear 186–187:487–492
4. Kennedy E, Byrne G, Collins DN (2004) A review of the use of high power diode lasers in surface hardening. J Mater Process Technol 155-156:1855–1860
5. Zhu J, Li L, Liu Z (2005) CO_2 and diode laser welding of AZ31 magnesium alloy. Appl Surf Sci 247(1–4):300–306
6. Cui C, Guo Z, Liu Y, Xie Q, Wang Z, Hu J, Yao Y (2007) Characteristics of cobalt-based alloy coating on tool steel prepared by powder feeding laser cladding. Opt Laser Technol 39:1544–1550
7. Laribi M, Vannes AB, Treheux D (2007) Study of mechanical behavior of molybdenum coating using sliding wear and impact test. Wear 262(11-12):1330–1336
8. Maiman TH (1969) Stimulated optical radiation in ruby. Essentials Lasers:134–136
9. Gnanamuthu DS (1980) Laser surface treatment. Opt Eng 19(5): 783–792
10. Jones DA (1992) Principle and prevention of corrosion, vol 208. Macmillan Publishing Company, New York
11. Chang JH, Chou JM, Hsieh RI, Lee JL (2010) Corrosion behavior of vacuum induction-melted Ni-based alloy in sulphuric acid. Corros Sci 52(7):2323–2330
12. Liu H, Wang C, Zhang X, Jiang Y, Cai C, Tang S (2013) Improving the corrosion resistance and mechanical property of 45 steel surface by laser cladding with Ni60CuMoW alloy powder. Surf Coat Technol 228:S296–S300
13. Xu P, Lin CX, Zhou CY, Yi XP (2014) Wear and corrosion resistance of laser cladding AISI 304 stainless steel/Al_2O_3 composite coatings. Surf Coat Technol 238:9–14
14. Qiwen W, Mingxing M, Cunyuan P, Xiaohui Y, Weiming Z (2013) Corrosion resistance of laser produced in-situ particle reinforced Fe-matrix composite coating with high nickel content on spheroidal graphite cast iron. Phys Procedia 41:276–281
15. Pacquentin W, Caron N, Oltra R (2014) Nanosecond laser surface modification of AISI 304L stainless steel: influence the beam overlap on pitting corrosion resistance. Appl Surf Sci 288:34–39
16. Xie F, He X, Cao S, Mei M, Qu X (2013) Influence of pore characteristics on microstructure, mechanical properties and corrosion

resistance of selective laser sintered porous Ti-Mo alloys for biomedical applications. Electrochim Acta 105:121–129
17. Vora HD, Rajamore RS, Dahotre SD, Ho Y-H, Banerjee R, Dahotre NB (2014) Integrated experimental and theoretical approach for corrosion and wear evaluation of laser surface nitride, Ti-6Al-4V biomaterial in physiological solution. J Mech Behav Biomed Matr 37:153–164
18. Jones RL (1997) Some aspects of the hot corrosion of thermal barrier coatings. J Therm Spray Technol 6:77–84
19. Mori T, Kuroda S, Murakami H, Katanoda H, Sakamoto Y, Newman S (2013) Effects of initial oxidation on β phase depletion and oxidation of CoNiCrAlY bond coatings fabricated by warm spray and HVOF processes. Surf Coat Technol 221:59–69
20. Zang Z (2013) All-optical switching in Sagnac loop mirror containing an ytterbium-doped fiber and fiber Bragg grating. Appl Opt 52: 5701–5706
21. Zang Z, Zhang Y (2012) Analysis of optical switching in a Yb3+ −dopped fiber Bragg grating by using self-phase modulation and cross-phase modulation. Appl Opt 51:3424–3430
22. Stefanov P, Atanasova G, Stoychev D, Marinova T (2004) Electrochemical deposition of CeO_2 on ZrO_2 and Al_2O_3 thin films formed on stainless steel. Surf Coat Technol 180-181:446–449
23. Go D, Shen Y (2008) The role of La_2O_3 in direct laser sintering of submicrometre WC-Co_p/Cu MMCs. J Phys D Appl Phys 41:1–11
24. Wang KL, Zhang QB, Sun ML, Wei XG, Zhu YM (2001) Rare earth elements modification of laser-clad nickel-based alloy coatings. Appl Surf Sci 174(3–4):191–200
25. Wang KL, Zhang QB, Sun ML, Wei XG, Zhu YM (2001) Microstructure and corrosion resistance of laser clad coatings with rare earth elements. Corros Sci 43(2):255–267
26. Surajit Purkayastha, D. K. Dwivedi (2012) Effect of CeO_2 on the friction and sliding wear performance of Ni/WC coatings. International Conference on Advances in Electrical And Mechanical Engineering Phuket Thailand 18–19
27. Handbook, Metals. Vol. 2 ASM Materials Par. OH (1990)
28. Farahmand P, Kovacevic R (2015) Corrosion and wear behavior of laser cladded Ni-WC coatings. Surf Coat Technol 276:121–135
29. Qu S, Pang X, Wang Y, Gao K (2013) Corrosion behavior of each phase in low carbon microalloyed ferrite-bainite dual-phase steel: experiments and modeling. Corros Sci 75:67–77
30. Argade GR, Kandasamy K, Panigrahi SK, Misra RS (2012) Corrosion behavior of a friction stir processed rare-earth added magnesium alloy. Corros Sci 58:321–326
31. Argade GR, Panigrahi SK, Misra RS (2012) Effects of grain size on the corrosion resistance of wrought magnesium alloys containing neodymium. Corros Sci 58:145–151
32. Arunas Baltusnikas, Rimantas Levinskas (2006) XRD analysis of carbide phase in heat resistant steels. Mater Sci Vol. 12, No. 3 1392–1320
33. Wang KL, Zhang QB, Sun ML, Wei XG (2003) Microstructural characteristics of laser clad coatings with rare earth metal elements. J Mater Process Technol I39:448–452
34. Scott A Speakman. Introduction to X-ray power diffraction data analysis. Massachusetts Institute of Technology
35. Jiang X, Zhao J, Jiang X (2011) Correlation between hardness and elastic moduli of the covalent crystals. Comput Mater Sci 50(7): 2287–2290
36. Smith WF (1981) Structure and properties of engineering alloys. McGraw-Hill Book Company, New York
37. Tian Y, Xu B, Zhao Z (2012) Microscopic theory of hardness and design of novel superhard crystals. Int J Refract Met Hard Mater 33: 93–106
38. Rajamore RS, Vora HD, Gupts N, Karewar S, Srinivasan SG, Dahotre NB (2014) Laser surface alloying of molybdenum on aluminum for enhanced wear resistance. Surf Coat Technol 258:337–342
39. Rajamore RS, Vora HD, Srinivasan SG, Dahotre NB (2015) Laser alloyed Al-W coatings on aluminum for enhanced corrosion resistance. Appl Surf Sci 328:205–214
40. Sharma SP, Dwivedi DK, Jain PK (2009) Effect of La_2O_3 addition on the microstructure, hardness and abrasive ear behavior of flame sprayed Ni based coatings. Wear 267:853–859
41. de Carvalho Fernandes SM, Ramanathan LV (2004) Rare earth oxide coatings to decrease high temperature degradation of Chromia forming alloys. Mat Res 7(1):135–139
42. Farahmand P, Liu S, Zhang Z, Kovacevic R (2014) Laser cladding assisted by induction heating of Ni-WC composite enhanced by nano-WC and La_2O_3. Ceram Int 40 (15421–15438
43. Shon Y, Joshi SS, Katakam S, Rajamore RS, Dahotre NB (2015) Laser additive synthesis of high entropy alloy coating on aluminum: corrosion behavior. Mater Lett 142:122–125